Geothermics 88 (2020) 101879

Contents lists available at ScienceDirect

Geothermics

journal homepage: www.elsevier.com/locate/geothermics

Stochastic workflows for the evaluation of Enhanced Geothermal System (EGS) potential in geothermal greenfields with sparse data: the case study of Acoculco, Mexico

Paromita Deb[a,*], Dominique Knapp[b], Gabriele Marquart[a], Christoph Clauser[a], Eugenio Trumpy[c]

[a] Institute for Applied Geophysics and Geothermal Energy, RWTH Aachen University, Aachen 52074, Germany
[b] Geophysica Beratungsgesellschaft mbH, Aachen 52064, Germany
[c] Institute of Geosciences and Earth Resources, National Research Council of Italy, Pisa 56124, Italy

ARTICLE INFO

Keywords:
Acoculco
Mexico
Hot Dry Rock
Enhanced Geothermal Systems
Stochastic simulation
Uncertainty quantification
Transient simulation

ABSTRACT

This paper presents a workflow for resource characterization and assessment of exploration geothermal fields with minimum data. Our approach utilizes stochastic methods to estimate the temperature distribution at potential target depths by focusing on the impact of uncertain input parameters such as thermal conductivity and porosity. We first perform stochastic forward simulations to determine the initial steady-state thermal field and subsequently quantify the uncertainty via a Monte Carlo approach known as Sequential Gaussian Simulation (SGSim). Next, we analyze the in-field likelihood of success for Enhanced Geothermal Systems by simulating hypothetical energy production scenarios based on existing geothermal installations. This approach is applied to the case study of a Hot Dry Rock geothermal field with two exploration wells, located in Acoculco, Mexico. Data scarcity in this field necessitates the use of stochastic methods for plausible prediction of reservoir temperature used to determine the accessible thermal power. Once reliable temperature estimates are obtained at potential target depths, we simulate production scenarios by assuming a prior successful stimulation process in the existing wells. In addition to providing preliminary estimates of thermal power for different injection/production rates, stimulated volumes and created permeability, we present the long-term impact of production on the temperature and pressure fields.

1. Introduction

Generation of electricity from geothermal energy has been until recently limited mostly to areas where natural convective systems drive the circulation of high temperature fluid. These systems are mostly dominated by wet steam or water, with temperatures ranging from 100 °C to 300 °C. Examples of such high-enthalpy permeable reservoirs, which have been commercially exploited, include Larderello, in Italy, Los Humeros, in Mexico and Krafla, in Iceland. Larderello is an example of a super-hot steam-dominated reservoir at relatively shallow depths (Minissale, 1991), whereas Los Humeros and Krafla are examples of geothermal systems with liquid-dominated, and two-phase zones at different depths (Arellano et al., 2003; Langella et al., 2017). Such producing geothermal fields are mostly characterized by naturally occurring permeable pathways, as faults and fractures, as well as by secondary porosity related to geochemical processes in the host rock, which contribute to abundant fluid circulation in the reservoir. These hydrothermal systems are, however, rare and concentrated around active volcanic zones and tectonic boundaries, whereas a vast resource of geothermal energy is trapped in areas with high heat flow but characterized by relatively tight (low porosity and low permeability) rocks, generally referred to as hot dry rock (HDR). It is estimated that the total amount of heat within drillable depths in HDR systems worldwide is in the order of 293×10^8 TW h (Brown et al., 2012). While this estimation is based on highly optimistic assumptions, nevertheless, it indicates the potential of HDR as a significant energy resource.

Energy from HDR systems can be extracted using enhanced or engineered geothermal systems (EGSs) techniques, which involves creating heat exchange areas within the hot rock mass by activating existing fracture networks or creating new pathways by a technique commonly known as hydraulic stimulation. The fluid injected into the reservoir is heated up in the heat exchange areas and then produced at the surface using a doublet or triplet system of wells, feeding a power plant for electricity or heat generation. EGS techniques are, however,

* Corresponding author.
E-mail address: pdeb@eonerc.rwth-aachen.de (P. Deb).

https://doi.org/10.1016/j.geothermics.2020.101879
Received 26 November 2019; Received in revised form 31 March 2020; Accepted 6 May 2020
Available online 17 June 2020

still under extensive research and development and therefore only few examples of actually operating EGSs installations are available, viz., Soultz-sous Forêts and Rittershoffen power plants in France, which came into operation in 2009 and 2016, respectively. Both the EGS sites were previously explored by the oil industry and therefore the geology was well-characterized (Kölbel and Genter, 2017; Baujard et al., 2017). Another, partly successful EGS project, Habanero Pilot Plant in South Australia, was recently discontinued due to economic reasons despite its technical effectivity (Llanos et al., 2015; Hogarth and Holl, 2017).

Due to economic and technological challenges associated with exploration, drilling and stimulation methods, EGS techniques are still not commercially viable. Moreover, the initial high-costs associated with proving resources prevent the acquisition of data required for adequate geological characterization. It is therefore necessary to develop workflows which can be used for initial resource assessment in fields with minimum data.

Acoculco, one of the geothermal exploration sites located in Mexico is investigated within the framework of the European Horizon 2020 project GEMex (Jolie et al., 2018). Using Acoculco as a case study, we present a workflow that can serve to evaluate the geothermal potential of similar greenfields with minimum available data. We first determined the initial steady-state temperature of the target geothermal reservoir using a stochastic workflow, which assesses the impact of uncertain parameters. Following this, we extracted the mean temperature at specific depths and evaluated the production potential of Acoculco, assuming that the existing exploration wells in this field are operated as a geothermal doublet. Similar studies directed towards estimating production capacity from EGS (Megel and Rybach, 2000; Sanyal and Butler, 2005) were performed, where the stimulated zone was modeled using discrete fracture network (DFN) models, investigating the effect of variable fracture parameters on production. In this study, we considered the stimulated zone as a fractured rock mass with increased permeability and investigated the effect of variable stimulation volumes and variable equivalent fracture permeability on the production capacity.

2. Thermal and Geological Data

Acoculco geothermal field is located in the Mexican federal state of Puebla in the eastern part of the Trans-Mexican Volcanic Belt, at an elevation of around 2850 m above sea level (Fig. 1). The area is characterized by presence of young volcanic rocks such as rhyolites, dacites, basalts and ignimbrites and extensive zones of hydrothermal alterations (López-Hernández et al., 2009). Thermal manifestations in form of acid springs, hydrothermal alterations and gas discharges have spurred interests in this area in the early 1980s. On the basis of helium isotope studies, Polak et al. (1982) associated this observed hydrothermal

Fig. 1. Relief map (Creative Commons 3.0, 2017) showing the Trans-Mexican Volcanic Belt (red), Mexico city (blue dot) and the location of Acoculco field (black square box).

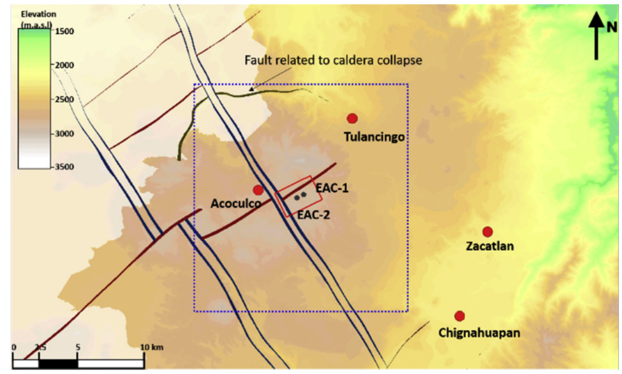

Fig. 2. Elevation map (after INEGI, Mexico) of the Acoculco geothermal field and location of the exploratory wells, EAC-1 and EAC-2 (black dots). Dominant regional fault trends (after Calcagno et al., 2018): normal faults (NE-SW), strike to oblique slip faults (NW-SE) and faults due to caldera collapse. Model boundaries: blue rectangle used for stochastic simulations (see section 4) and red rectangle for transient thermal simulations (see section 5).

activity with the presence of an active magmatic source at depth. As a result, preliminary investigations were conducted by CFE in 1983 as part of a regional exploration program (López-Hernández et al., 2009).

After further geological and geochemical investigations in this area, CFE drilled a first exploration well (EAC-1) in 1987 (Fig. 2). This vertical well encountered a temperature of around 300 °C at a depth of 2000 m (Pulido et al., 2010). In 2008, a second exploration well (EAC-2) was drilled and similarly a high temperature was observed. According to the drilling reports, negligible circulation losses were recorded during drilling of EAC-1, whereas EAC-2, located less than 500 meters east of EAC-1, exhibited circulation losses of around 20 m^3/h – 30 m^3/h at a depth of 1840 m (Pulido et al., 2010). These observed losses could in effect relate to the neighboring fault systems (Fig. 2), which were inferred from the geophysical data (López-Hernández et al., 2009).

CFE performed temperature and pressure logging in both wells (Fig. 3). In EAC-1 temperature data were logged 6, 12, 18 and 24 hours after drilling and pressure after 6 and 24 hours. Additionally, two heating-up surveys were performed after a shut-in period of 288 hours (12 days) and 312 hours (13 days). The two temperature logs were nearly coincident suggesting that the borehole was equilibrated with the surrounding formation (Fig. 3a).

From the temperature records of EAC-1, a sharp change in temperature gradient was recorded at a depth of 1600 m. This gradient change is probably due to a change in lithology from skarn to granite. The average temperature gradient in the skarn and in the granite based on the data obtained from the warm-up stage are 132 mK m^{-1} and 164 mK m^{-1}, respectively.

In EAC-2, no temperature or pressure records were taken after a longer shut-in period. Therefore, the static formation temperature at bottom-hole depth was calculated from temperature measurements after drilling, using the spherical radial heat-flow (SRF) method (Ascencio et al., 1994).

Temperature data in well EAC-2 show a similar gradient change as to the one in EAC-1 at a depth of around 1660 m below surface, also suggesting a change in lithology (Fig. 3b). At a depth of 1842 m, where fluid losses were observed, the temperature logs show a further abrupt change in gradient. However, in absence of additional measurement points and heating-up surveys, it is not clear whether this is the result of a local convection zone, or an indication of a shallow magmatic intrusion (e.g. young dike). Based on the available information from drilling and temperature data, the field can be classified as a low-permeability conduction-dominated field.

The main lithologic units of well EAC-1 and EAC-2, derived from drill cuttings, consist of volcanic rocks belonging to different volcanic

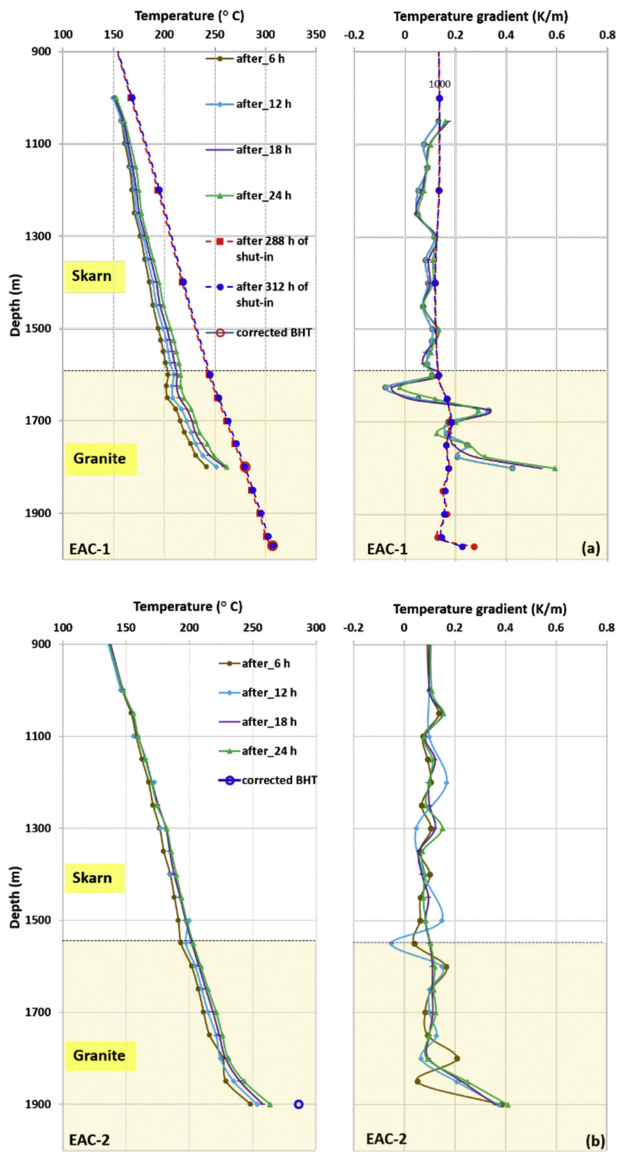

Fig. 3. Temperature (left) and temperature gradient (right) in wells EAC-1 (a) and EAC-2 (b), observed in the depth interval 900 m – 2000 m, from temperature measurements performed at different times after drilling (solid curves) and in EAC-1 after the warm-up stage (dashed curves). The corrected bottom hole temperature for EAC-1 (red empty circle) and EAC-2 (blue empty circle) are also shown.

episodes (between 3 and 1.3 million years) resting on a thick metamorphic sequence. This metamorphic sequence is made up of skarn and marble and is the product of contact metamorphism due to the emplacement of mid-Tertiary granitic intrusions into the Cretaceous limestone of Sierra Madre Oriental (López-Hernández et al., 2009; Pulido, 2010). These granitic intrusions are not exposed at the surface, but were intersected by both wells and considered as possible sources of the observed temperature anomaly.

López-Hernández et al. (2009) provide a detailed evaluation of the available geophysical data (gravity, magnetic, DC-resistivity and magnetotelluric) in this area from which the structure of the Tulancingo - Acoculco caldera complex was derived. The geometry of the caldera and the main regional fault trends, inferred from gravity, magnetic and magnetotelluric data, were supported by morphological evidence, such as the alignment of volcanic cones along the major lineaments. The study of the volcanic rocks of the region indicated that the caldera complex is associated with two major volcanic episodes (López-Hernández et al., 2009). The first one, active between 3 and 2.7 million years ago, resulted in a caldera collapse of diameter 32 km and is referred to as Tulancingo caldera, whereas the second volcanic activity from 1.7 million to 240 thousand years ago gave rise to the younger Acoculco caldera with a diameter of 18 km.

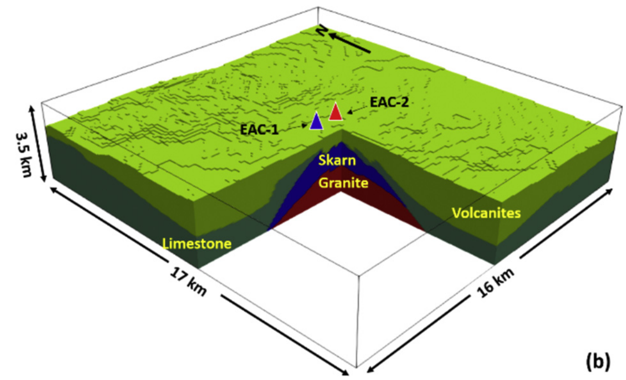

Fig. 4. Structural model of the Acoculco geothermal field with the main lithological units, wells and model dimensions (see also Fig. 2 for location).

The major regional fault systems (Fig. 2) recognized in this area are mutually cross-cutting: the NE-SW oriented normal fault system and the NW-SE trending strike to oblique slip faults (Calcagno et al., 2018). The latter post-date (Late-Cretaceous to Early Tertiary) the compressive deformation event that created the Sierra Madre Oriental fold belt (López-Hernández et al., 2009). Minor E-W trending faults associated with the Acoculco caldera evolution are also reported from field investigations. (López-Hernández et al., 2009). Well information (Pulido et al., 2010) combined with surface geology and a geological map of Avellán et al. (2018) were used to build a simplified regional geological model of Acoculco area within the GEMex project (Calcagno et al., 2018, 2021). The geological model used in this study (Fig. 4) was extracted from this regional-scale model.

3. Governing Equations

In a porous medium, conservation of mass is expressed by the continuity equation

$$\partial(\varphi \bullet \rho_f)/\partial t + \nabla \bullet (\rho_f \bullet \boldsymbol{v}) = 0, \tag{1}$$

where φ is the porosity and ρ_f is the density of the fluid (kg m^{-3}); $\mathbf{v}$ is the Darcy velocity or specific discharge (m s^{-1}) defined by Darcy's law as

$$\boldsymbol{v} = -\frac{\underline{k}}{\mu_f}(\nabla p + \rho_f g \nabla z), \tag{2}$$

where $\underline{k}$ is the permeability tensor (m^2), μ_f is the dynamic viscosity (Pa s) of the pore fluid, g the acceleration due to gravity (m s^{-2}) and z is the vertical depth (m). The fluid pressure p (Pa) is calculated according to the vertical head distribution h (m) and depth z

$$p(z, h) = p_0 + \int_0^z \rho_f(\tilde{z}) g (h - \tilde{z}) \Big) d\tilde{z}, \tag{3}$$

where p_0 represents the pressure at the surface (z = 0). The symbol p_b is used to refer to the pressure (3) calculated in the individual grid blocks.

The steady-state heat transport equation (4) defines the heat generation H (W m^{-3}) as composed of two terms

$$(\rho c)_f \boldsymbol{v} \nabla T - \nabla \bullet (\lambda_e \nabla T) = H \tag{4}$$

An advective term with specific discharge $\boldsymbol{v}$, where $(\rho c)_f$ is the thermal capacity of the fluid (J m^{-3} K^{-1}) and T the temperature (°C), and a conductive term, in which the effective thermal conductivity of the rock-fluid mixture λ_e (W m^{-1} K^{-1}) is assumed to be isotropic.

Effective thermal conductivity λ_e of the fluid-filled porous rock depends on the porosity ϕ, fluid thermal conductivity λ_f and rock matrix thermal conductivity λ_m according to the relation

$$\lambda_e = \lambda_f^{\phi} \lambda_m^{(1-\phi)}. \tag{5}$$

Rock matrix thermal conductivity λ_m depends on the rock type, but generally decreases with temperature (Zoth and Hänel, 1988). A correction for matrix thermal conductivity λ_m with temperature T was performed according to the equation proposed by Sekiguchi (1984). Lee and Deming (1998) demonstrated the suitability of this equation for obtaining corrected λ_m values for igneous and metamorphic rocks in temperature conditions ranging between 0 °C and 500 °C. The adopted formula, based on a given matrix conductivity at room temperature $\lambda_{m,0}$ and temperature T, is given by (Chiozzi et al., 2017):

$$\lambda_m(T) = a + (\lambda_{m,0} - a)\left(\frac{1}{b \cdot T + c} - d\right)$$
$$a = 1.8418$$
$$b = 0.002732$$
$$c = 0.7463$$
$$d = 0.2485 \tag{6}$$

The fluid properties in sub-critical and super-critical conditions were calculated using the correlations provided by the International Association for the Properties of Water and Steam (Wagner et al., 2000).

For transient simulations in the stimulated reservoir volume, the following formulations for thermal power P_t, bottom hole pressure (BHP) p_w and reservoir impedance i are implemented in the code SHEMAT-Suite.

The thermal power P_t of a geothermal doublet installation is calculated using the following formulation

$$P_t = \rho_f c_p \Delta T Q, \tag{7}$$

where c_p is the specific heat capacity of the fluid (J kg^{-1} K^{-1}), assumed constant throughout the simulation for mass balance. ΔT is the temperature difference (K) between the produced and injected fluid and Q is the flow rate (m^3 s^{-1}). It is assumed that there is no heat loss to the surroundings when the hot water ascends through the cooler rocks.

The BHP of a flowing well p_w cannot be assumed equal to the fluid pressure p_b calculated in the discretized grid blocks (using equation (3)). This is because the dimensions of the grid blocks (Δ x and Δ y) are much greater than the actual radius of the borehole r_w. Therefore, using the semi-analytical approach introduced by Peaceman (1983), we compute the well pressure from the grid block pressure as

$$p_w = p_b - \frac{Q\mu_f}{2\pi k \Delta z} ln\left(\frac{r_b}{r_w}\right), \tag{8}$$

r_b is the equivalent radius of a well with pressure p_b, expressed with respect to the grid size as

$$r_b = 0.14 \bullet (\Delta x^2 + \Delta y^2)^{1/2}. \tag{9}$$

It is to be noted that close to an injection or production well, non-laminar or turbulent flow may occur. To identify such flow patterns, it is necessary to compare the simulated pressure and Darcy velocity to the actual reservoir values. However, in absence of such information, initial approximations of pressure and temperature field in the exploration block are usually calculated under the assumption of laminar flow conditions (e.g., Kolditz and Clauser, 1998; Vogt, 2013).

The reservoir impedance i is one of the key parameters that determines the economic feasibility of a project. It is defined in (10) as the pressure difference (Pa) required to circulate a certain flow rate (L s^{-1}) through the stimulated permeable zone, calculated using the pressure at the injection p_{wi} and production p_{wp} intervals (e.g., Kolditz and Clauser, 1998).

$$i = \frac{p_{wi} - p_{wp}}{Q} \tag{10}$$

To ensure economic feasibility of a project, the reservoir impedance should not exceed 100 kPa s L^{-1} (e.g. Clauser, 2006).

4. Thermal Model

The geological structure used for the stochastic simulations in Acoculco is shown in Fig. 4. The potential reservoir extent was selected large enough to be centered on the granitic intrusion and, at the same time, small enough to keep the simulation run time within reasonable limits. The geological model has a dimension of 16 km × 17 km × 3.5 km and its deepest vertical limit coincides with the mean sea level. The grid cells are equal-sized with a dimension of 150 m × 150 m × 50 m, yielding a total of 846370 cells.

At the top of the model, a Dirichlet boundary condition was assigned with a constant temperature of 12 °C, while at the bottom of the model domain, Neumann boundary condition with variable heat flow was assigned. The regional heat flow in the TMVB is about 91 mW m^{-2} (Ziagos et al., 1985). However, a higher heat flow was applied under the granitic intrusion based on well information. A value of about 390 mW m^{-2} was determined by an iterative approach that aims to minimize the differences between the static temperature measurements from wells EAC-1 and EAC-2 and the simulated temperatures. For each heat flow value in the investigated range between 360 mW m^{-2} and 400 mW m^{-2}, an error was defined as the sum of the squared errors (SSE) between all the available control points T_w and the relative simulated temperatures T_s evaluated at the same depths. Thus, the heat flow HF_{sim} adopted as boundary condition under the granitic intrusion for the stochastic simulations was the value that minimized the SSE.

4.1. Model parameters estimation

As in any other exploration field, one of the major challenges in Acoculco is the level of uncertainty associated with reservoir properties. In fact, due to the absence of petrophysical logs and good-quality core samples from the wells, physical properties of the rock formations were primarily determined from measurements on outcrop analogues and literature data. However, as reported in Bär et al (2019), the sampled outcrop analogues from Acoculco do not represent all the units of the geological model, and may also suffer from sampling bias. Additionally, the samples are affected by varying degree of hydrothermal alteration. For this reason, the proposed workflow is used to evaluate the effect of poor knowledge of rock properties (reported in Table 1) on the simulated formation temperature.

To this end, we used the Monte Carlo approach of Sequential Gaussian Simulation (SGSim; Deutsch and Journel, 1998), which uses the statistical information of measured rock properties to generate equally probable realizations of petrophysical models. The SGSim uses the Kriging interpolation technique to assign values to each grid node based on neighboring data and already simulated grid nodes. This computation is controlled by the rock properties distribution and their

Table 1
Average value, μ, and standard deviation, σ, of porosity, ϕ, and thermal conductivity, λ_m, of rocks obtained from laboratory measurements on outcrop samples (data sources: Deb et al. (2019), Bär et al (2019), Schön (2004) and (1976, 1986).

Rock type	ϕ (%)		λ_m (W m^{-1} K^{-1})	
	μ	σ	μ	σ
Volcanite	11.20	2.02	2.50	0.19
Limestone	1.17	1.40	2.90	0.26
Skarn	1.22	0.60	3.89	0.60
Granite	2.00	0.25	3.20	0.25

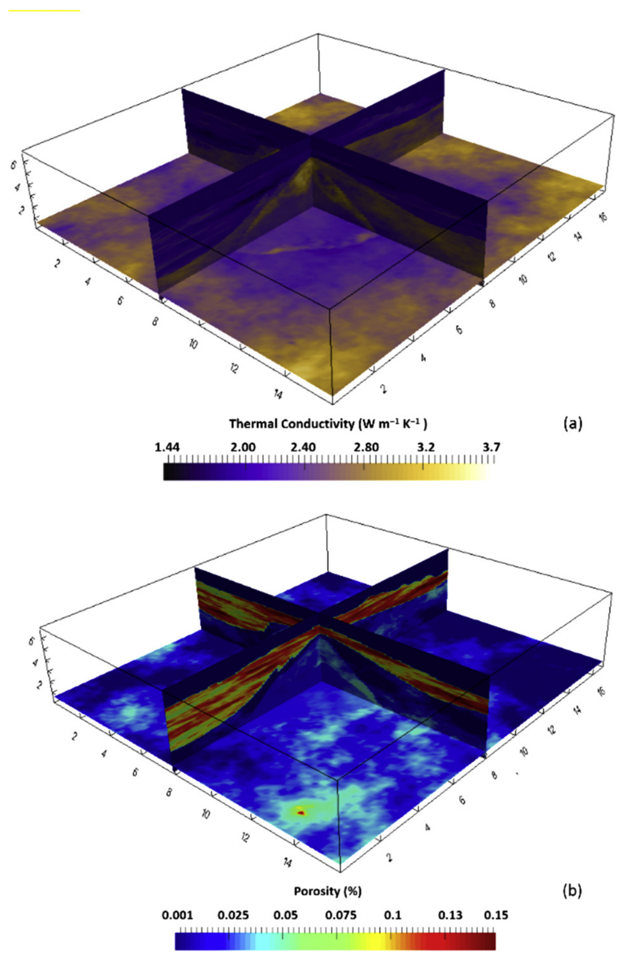

Fig. 5. Examples of matrix thermal conductivity and porosity from one realization of stochastic simulation in the Acoculco geothermal field (see also Fig. 4 for the model layout).

correlation lengths, which determine the spatial relationship of rock properties in the field. In our approach, parameters that govern the heat conduction process, such as matrix thermal conductivity and porosity, were treated as random variables $\hat{\lambda}_m$ and $\hat{\phi}$ respectively, and varied stochastically to generate a normally distributed population of 1000 values. For lack of sufficient representative samples from Acoculco site, the rock property distribution was assumed as normally distributed analogous to the distribution observed in the neighboring geothermal field, Los Humeros (Bär et al., 2019).

To assess both the individual and combined effects of rock property uncertainty on temperature, we performed three sets of stochastic simulations. The first set was performed by varying only the matrix thermal conductivity $\hat{\lambda}_m$ according to the assigned probability density function. Similarly, we assessed the individual impact of uncertain porosity $\hat{\phi}$ in the second set of simulation. In the third set of simulations, we stochastically varied both thermal conductivity and porosity at the same time to investigate the combined effect on the simulated temperature. Fig. 5 shows examples of models of stochastically distributed thermal conductivity and porosity obtained from a single realization.

In addition to rock property histograms, correlation lengths are essential parameters for determining the spatial relationship of rock properties. In general, petrophysical well-log data and any other good resolution geophysical data (e.g., seismic) provide estimates of vertical and horizontal correlation lengths. In absence of such data in Acoculco, which could provide usable constraints on geological correlation lengths, it was necessary to investigate the impact of different correlation lengths on the temperature field.

For each set of stochastic simulations, we tested three scenarios, where correlation lengths for each rock unit were varied. In the basic scenario, denoted as scenario L, we considered a correlation length of 1500 m in horizontal direction and 100 m in vertical direction for the volcanite unit. These correlation lengths were assumed to represent the nature of the volcanic deposits, in which properties among different flow units are expected to change strongly in the vertical direction. The platform deposits of the Cretaceous limestone were considered as the regional basement in Acoculco as well as in the neighboring geothermal fields like Los Humeros (López-Hernández et al., 2009). Considering its regional extent and layered structure, a minimum horizontal correlation length of 1500 m and a vertical correlation length of 500 m was assigned. The skarn unit, which is not a layered structure but rather dependent on metamorphism and emplacement of dykes, was assumed to have a correlation length of 500 m, both horizontally and vertically. The granite intrusion was considered as the most homogeneous unit and hence the parameters were distributed using a correlation length of 3000 m in all directions.

To investigate the effect of variable correlation lengths on the temperature field, we halved the correlation length in each direction in scenario L/2, whereas, in scenario 2 L we doubled the correlation length assumed in scenario L. In all simulations a spherical variogram without specific search angle was used. A summary of horizontal and vertical correlation lengths used for the different scenarios is reported for sake of clarity in Table 2.

4.2. Sensitivity Analysis

The Monte Carlo-SGSim approach generates a set of equally likely models of the subsurface based on input data and geological knowledge. For each scenario listed in Table 2 an ensemble of 500 realizations was generated by performing stochastic steady-state forward simulations. These realizations were then used for simulating heat transfer and fluid flow using the finite differences code SHEMAT-Suite (Rath et al., 2006; Clauser, 2003).

The temperature differences among the nine scenarios are presented in Table 3. Ensemble mean temperatures and standard deviations were extracted at the top and bottom depths of the skarn and the granite units, at the locations of wells EAC-1 and EAC-2. The mean temperature calculated at the unit interfaces does not show significant changes by varying either correlation lengths or rock properties. Conversely, the standard deviation of the simulated temperature profiles exhibits a direct correlation (Fig. 6) with increasing correlation lengths and a stronger sensitivity towards thermal conductivity rather than porosity variations, with an intermediate behavior observed in all the cases for joint variations of the two parameters.

For increasing correlation length, the SGSim interpolation algorithm distributes the rock properties rather uniformly, thus resulting in 500 models with a quasi-homogeneous distribution of properties. Therefore, the simulated temperature distribution at a specific location results in a stronger variation, reflecting the dispersion in input rock properties. In case of smaller correlation lengths, the rock properties are distributed in a more heterogeneous manner in every realization,

Table 2
Assumed values of correlation lengths (m) in the different stochastic simulation scenarios (H = horizontal, V = vertical).

Scenarios		Volcanites	Limestones	Skarn/ Marble	Granite
Scenario L	H	1500	1500	500	3000
	V	100	500	500	3000
Scenario L/2	H	750	750	250	1500
	V	50	250	250	1500
Scenario 2 L	H	3000	3000	1000	6000
	V	200	1000	1000	6000

Table 3
Mean temperature (°C) and standard deviation (K) extracted at the top and bottom depths of the skarn and the granite reservoir units while varying a specific parameter. Values at specific depths are averaged between the well locations of EAC-1 and EAC-2.

	Depth (m)	Rock type	Scenario L/2	Scenario L	Scenario 2 L
$\hat{\lambda}_m$	450	Skarn	92.13 [1.00]	92.14 [1.60]	92.21 [2.36]
	1200	Skarn	179.40 [1.10]	179.34 [1.90]	179.22 [3.01]
	1550	Granite	221.67 [1.29]	221.55 [2.07]	221.41 [3.40]
	2300	Granite	330.64 [1.50]	330.58 [2.50]	330.41 [4.37]
$\hat{\phi}$	450	Skarn	91.29 [0.23]	91.28 [0.44]	91.24 [0.74]
	1200	Skarn	178.45 [0.18]	178.45 [0.42]	178.41 [0.82]
	1550	Granite	221.05 [0.20]	221.02 [0.41]	220.99 [0.84]
	2300	Granite	329.72 [0.27]	329.69 [0.48]	329.64 [0.97]
$\hat{\lambda}_m$, $\hat{\phi}$	450	Skarn	91.28 [1.00]	91.25 [1.26]	91.31 [1.78]
	1200	Skarn	179.74[0.95]	179.62 [1.56]	179.49[2.29]
	1500	Granite	222.98 [1.10]	222.83[1.70]	222.64 [2.71]
	2300	Granite	332.24 1.20]	332.10[2.17]	331.95[3.18]

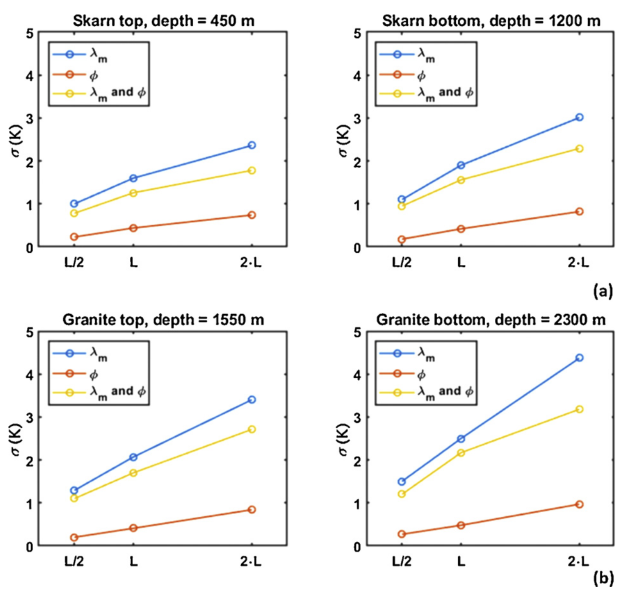

Fig. 6. Standard deviation σ in simulated temperatures as a function of correlation length (scenarios L/2, L and 2L) and varying rock properties ($\hat{\lambda}_m$and $\hat{\phi}$), calculated at the top and the bottom interfaces of skarn (a) and granite units (b).

resulting in an averaging effect in simulated temperature that, in turn, reduces the overall standard deviation of simulated temperatures.

When analyzing the effect of rock properties (Table 3 and Fig. 6), it is observed that the effect of thermal conductivity is much larger than porosity. This is due to the overall low porosity of the lithotypes occurring at Acoculco. For example, in the Scenario L, the temperature standard deviation at the bottom of the skarn unit is 1.9 K when only varying $\hat{\lambda}_m$, with a sensitivity coefficient given by the ratio of the relative standard deviation of temperature to that of thermal conductivity of 6.86 %. Similarly, when only porosity is varied, the temperature standard deviation reduces to 0.42 K (with a sensitivity coefficient of 0.48 %), i.e. 14 times smaller than the one induced by varying thermal conductivity. An intermediate value of 1.56 K is obtained when varying both $\hat{\lambda}_m$ and $\hat{\phi}$ simultaneously due to the inverse correlation between the two.

4.3. Temperature Uncertainties

For calibration of the temperature models, we used the equilibrated temperature logs from warm-up surveys in EAC-1 and the corrected static temperature at bottom-hole depth in EAC-2. Fig. 7 shows a comparison between the simulated temperatures along well profiles EAC-1 and EAC-2 with those obtained by a classic deterministic approach. The case with the highest uncertainty is obtained with scenario 2 L of the third set of simulation, where both $\hat{\lambda}_m$ and $\hat{\phi}$ are varied simultaneously under the assumption of the highest correlation lengths.

The model envelopes representing the 99.7 % confidence intervals were obtained in deterministic case by performing forward simulations with constant rock parameters $\mu \pm c{\cdot}\sigma$, where $c = 3$ is the coverage factor associated with a level of confidence of 99.7% and μ and σ are the mean and standard deviation associated with the rock properties (Table 1). Conversely, the confidence intervals for the stochastic simulation were calculated with the same coverage factor after estimating the mean temperature and standard deviation over the 500 realizations.

The difference between the mean temperatures obtained with the stochastic models and the deterministic model are negligible (less than 2 K) over the entire depth range. Additionally, the RMSE of the stochastic mean with respect to the stabilized borehole temperature measurements does not exceed 3.6 K. However, the narrower confidence intervals of the stochastic simulations indicates an almost seven times higher confidence on the predicted temperature, highlighting the more reliable results obtained by the stochastic approach as compared to the classical deterministic approach.

5. EGS Potentials in Acoculco

According to current reservoir knowledge from the drilled wells and the recorded temperatures (Fig. 3), the primary targets for stimulation could be the thick basement layer which consists of skarn (Pulido et al., 2010) or the deeper granitic intrusion. In our simulation, we considered EAC-1 and EAC-2 as a geothermal doublet, whereby EAC-1 acts as injector and EAC-2 as producer. We considered a hypothetical scenario where both wells were successfully stimulated for production from the hot and impermeable skarn or granite. We defined the geometry and the hydraulic properties of the stimulated zone and then used these parameters to perform transient simulations for a production period of 30 years.

5.1. Geometry of the Stimulated Zone

To evaluate the performance of skarn and granite as reservoirs separately, we analyzed two different reservoir models, targeting the depths of skarn and granite. The numerical grid for the skarn reservoir model with the stimulation zone is shown in Fig. 8. It is assumed that stimulation process in the wells created a fractured volume, which connects both wells giving rise to a heat exchange area. The effective heat exchange area depends on the applied stimulation techniques and is a function of the length, width and average spacing between the fractures, which in reality may not act as separate discrete fractures, but rather as an overall fractured mass (MIT, 2006). In our reservoir model, we simplified the stimulated volume as an overall fractured mass with upscaled permeability. It is represented by a rectangular prism having a width of 100 m and a horizontal extent of 1150 m (Fig. 8), enough to ensure connectivity between the two wells to form a geothermal doublet. Although an assumption in this study, it is consistent with the extent of the hypocenter cloud resulting from the induced seismic events recorded during the stimulation of the well Habanero 4 (Llanos et al., 2015). To test the impact of variable stimulated volumes on pressure and temperature of the field, we investigated two hypothetical vertical lengths for the modeled stimulation zone: 100 m and 300 m. The choice of the lengths were motivated from Reinicke (2009), who provides a range for vertical length of fractures dependent on different stimulation techniques. The stimulated volumes in skarn and granite with a vertical length of 100 m are denoted as SSV1 and GSV1, respectively. Similarly, the stimulated volumes corresponding to vertical

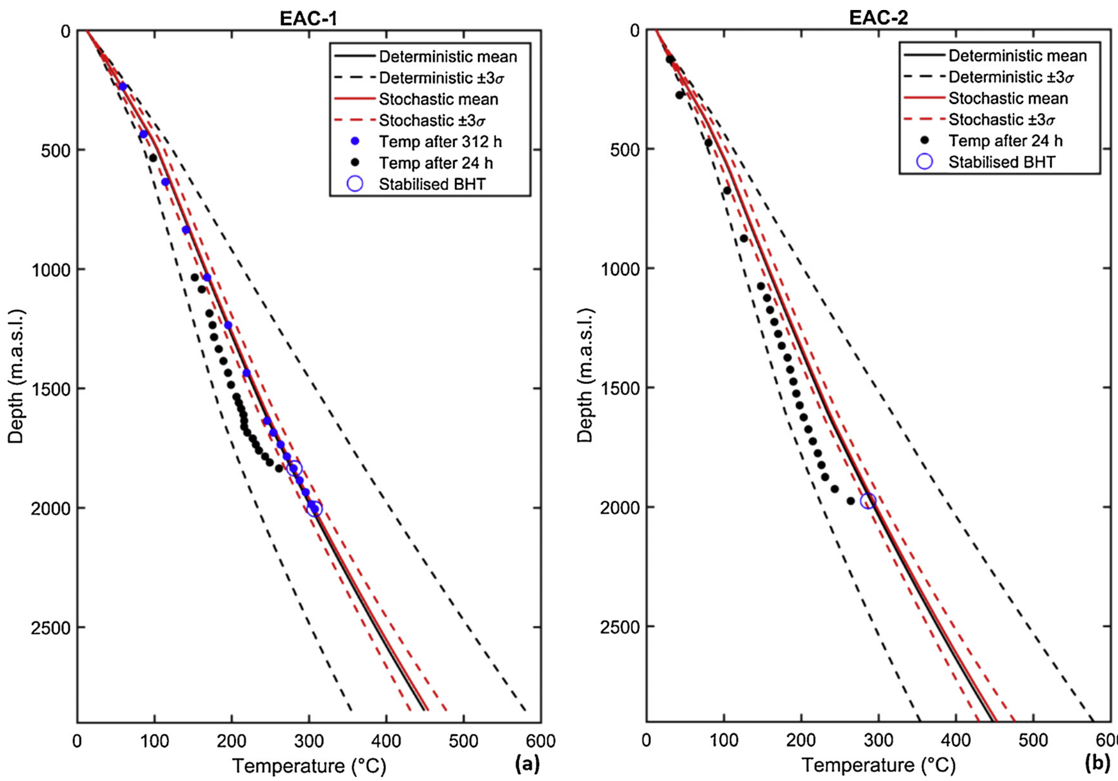

Fig. 7. Simulated temperature vs borehole temperature measurements for wells EAC-1 (a) and EAC-2 (b) (see text).

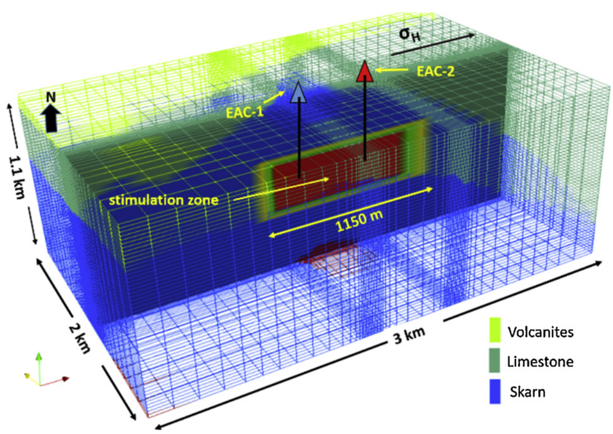

Fig. 8. Numerical grid for the thermal modeling within the skarn reservoir with boreholes EAC-1 and EAC-2 acting as injector and producer. Extension and position of the stimulated area (rectangular zone, in red) within the skarn reservoir (in blue) is shown.

length of 300 m are denoted as SSV2 and GSV2.

In accordance with the direction of the apparent maximum horizontal stress (Fig. 8) as inferred from the regional stress maps and regional fault trends (Liotta et al., 2019; Norini et al., 2019; Heidbach et al., 2016), the direction of the stimulated volume is aligned in NE-SW direction. The grid axes of the reservoir numerical model were accordingly rotated so that the principal axes were aligned with the directions of principal stresses. The meshing was refined in the proximity of the well locations to account for the higher fluid velocities at the producer and injector. Grid size varies from 10 m to 142 m in the x–direction and from 10 m to 135 m in the y–direction, while the discretization in z–direction is held constant at 20 m (Fig. 8).

5.2. Hydraulic Properties

The hydraulic and thermal properties used for the transient simulation are listed in Table 4. Before simulating the production scenarios, we computed the undisturbed temperature field for all four reservoir models by performing steady-state simulation. Temperature boundary conditions were extracted from the stochastic simulation results and assigned as a Dirichlet boundary condition. This steady state model was then used as initial model for the transient simulation.

We varied both permeability of the stimulation zone and flow rate to understand their impact on the temperature and pressure changes with time. We evaluated two production scenarios with permeability of the central stimulation zone in the order of 10^{-12} m^2 and 10^{-13} m^2. Away from the central stimulation zone, we assumed a decrease in the permeability by one order of magnitude in the first 40 m, followed by a further decrease of two orders of magnitude in the next 20 m and, finally, the permeability was set to 10^{-15} m^2 at the zone borders. Other studies have indicated a similar permeability range for similar EGS systems. In Soultz-Sous-Forêts, Vogt et al. (2012) provided estimates of permeability of the fractured zone in the order of 10^{-14} m^2 to 10^{-12} m^2 (10 md – 1000 md) evaluated using a tracer circulation test.

Apart from permeability and stimulation volumes, we simulated the performance of Acoculco EGS under three different flow rates constant over a period of 30 years: 10 L s^{-1}, 30 L s^{-1} and 50 L s^{-1}. The temperature of the injected fluid was set to 70 °C to inhibit mineral precipitation and clogging of the injection wells (Li and Lior, 2014). As SHEMAT-Suite allows only volumetric fluid input and output at the injector and producer cells, the fluid properties (density, specific heat capacity and dynamic viscosity) were set to a constant value to ensure mass balance (see Table 4). We assumed total water recovery and no loss to the formation.

5.3. Results and discussion

The effectiveness of a geothermal doublet is controlled by the

Table 4
Model properties for transient simulations on skarn and granite reservoir volumes.

Parameter	Skarn reservoir	Granite reservoir
Model size	3000 × 2000 × 1100 m^3	3000 × 2000 × 1100 m^3
Mesh size	61 × 40 × 55 m^3	61 × 40 × 55 m^3
Resolution	x: 10 m – 135 m	x: 10 m – 135 m
	y: 10 m – 142 m	y: 10 m – 142 m
	z: 20 m	z: 20 m
Stimulated volumes	1150 × 100 × 100 m^3	1150 × 100 × 100 m^3
	1150 × 100 × 300 m^3	1150 × 100 × 300 m^3
Temperature at reservoir top	91.25 °C	222.83 °C
Temperature at reservoir bottom	179.62 °C	332.10 °C
Simulation time	30 years	30 years
Permeability	10^{-12} m^2, 10^{-13} m^2	10^{-12} m^2, 10^{-13} m^2
Circulation rate	10 L s^{-1}, 30 L s^{-1}, 50 L s^{-1}	10 L s^{-1}, 30 L s^{-1}, 50 L s^{-1}
Temperature of injected water	70 °C (EAC-1)	70 °C (EAC-1)
Constant fluid dynamic viscosity*	2.06 × 10^{-4} Pa s (@ 135 °C)	9.58 × 10^{-5} Pa s (@ 283 °C)
Constant fluid density*	935.59 kg m^{-3} (@ 135 °C)	761.93 kg m^{-3} (@ 283 °C)
Constant fluid specific heat capacity*	4248 J kg^{-1} K^{-1} (@ 135 °C)	5079 J kg^{-1} K^{-1} (@ 283 °C)
Constant fluid thermal conductivity*	0.69 W m^{-1} K^{-1} (@ 135 °C)	0.59 W m^{-1} K^{-1} (@ 283 °C)

* calculated at reservoir pressure and temperature considering a salinity of 0 mg L^{-1} (IAPWS-IF97).

interplay of several factors, among which the most important ones are the initial rock temperature, effective heat-exchange area (geometry of the stimulation zone), circulation rate, and separation between the injector and producer wells (MIT, 2006). With a defined injector-producer distance in Acoculco, we present results of scenarios investigating the other influencing factors.

5.3.1. Skarn Reservoir

Development of an engineered geothermal reservoir in skarn is challenging, because skarns are hard and dense metamorphic rocks. to the best of authors' knowledge, no examples are available in literature of fractured skarn reservoirs producing geothermal energy. However, in Acoculco, the high temperature encountered in skarn at shallow depths presented a potentially favorable case for an EGS. Results in Fig. 9 illustrate the temperature, pressure and thermal power with time in response to production from the skarn reservoir for different injection rates, permeability and stimulation volumes.

In SSV1, which corresponds to a central stimulated volume of 0.012 km^3 (1200 m × 100 m × 100 m), the production temperature corresponding to higher flow rates of 30 L $s^{-1}$and 50 L s^{-1} decreases sharply and drops below 90 °C within 6 – 7 years of production. The corresponding average thermal power generated during this period is between 3 MW and 4 MW respectively for flow rates of 30 L $s^{-1}$and 50 L s^{-1}. With a flow rate of 10 L s^{-1}, which is rather uneconomic for commercial purposes, a thermal power of approximately 2.5 MW is generated for the first two years with production temperature around 135 °C, after which it starts declining and reaches 1 MW within 6 years. In the following years the thermal power output corresponding to all flow rates and permeability values produces a similar output between 1 MW – 1.5 MW. The impact of different permeability values is however reflected in the pressure response curves. In the low permeability scenario of SSV1, the pressure strongly declines after production begins for a flow rate of 50 L s^{-1} and drops below zero. This is caused due to insufficient recharge in the reservoir because of very low permeability. In reality, however, a negative pressure is not possible and therefore this scenario indicates a non-sustainable injection rate. Pressure curves corresponding to high permeability of 10^{-12} m^2 show negligible pressure decline irrespective of the flow rates indicating a balance between extraction and recharge into the reservoir. For SSV2, which corresponds to a larger stimulated volume of 0.036 km^3 (1200 m × 100 m × 300 m), the temperature declines more gradually as compared to SSV1. For an economic flow rate of 50 L s^{-1}, the temperature starts declining sharply after 1.5 years and approaches 95 °C after 6 years. Accordingly, the generated thermal power falls from 13 MW in the first 1.5 years to 4.5 MW within 6 years of production.

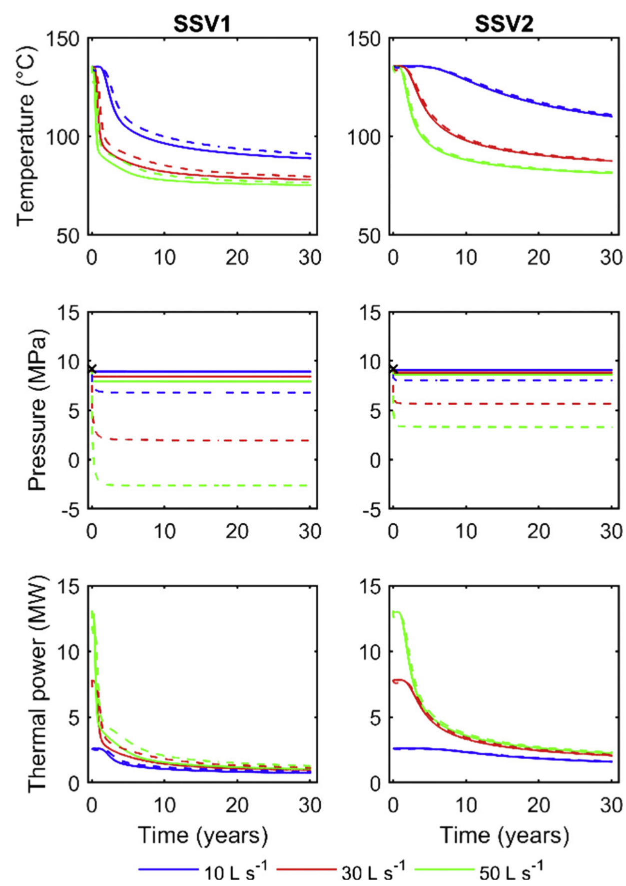

Fig. 9. Temperature (top), pressure (middle) and thermal power (bottom) for EGS in skarn reservoir with volumes SSV1 (left) and SSV2 (right) as a function of time, injection rates and permeability, 10^{-12} m^2 (solid lines) and 10^{-13} m^2 (dashed lines). The initial pressure is indicated by a black cross on the y axis.

Over this time period, the average generated thermal power is around 8.3 MW. The thermal power obtained in every scenario is directly related to the flow rates and to the output temperature at the production well, and shows negligible sensitivity towards different permeability values. However, the technical feasibility of a specific configuration is largely dependent on the pressure response of the reservoir, which is driven by the reservoir permeability. Even though the thermal power curves calculated for two different permeability scenarios overlay each

Table 5
Reservoir impedance *i* for different simulated volumes *V*, permeability *k* and flow rates *Q* in skarn

V	*k* (m^2)	*Q* ($L\ s^{-1}$)	*i* ($kPa\ s\ L^{-1}$)
SSV1	10^{-12}	10/ 30/ 50	57.71/ 57.90/ 58.19
SSV1	10^{-13}	10/ 30/ 50	532.67/535.91/ 533.33
SSV2	10^{-12}	10/ 30/ 50	25.38/ 25.42/ 25.50
SSV2	10^{-13}	10/ 30/ 50	248.8.33/ 249.10/ 249.95

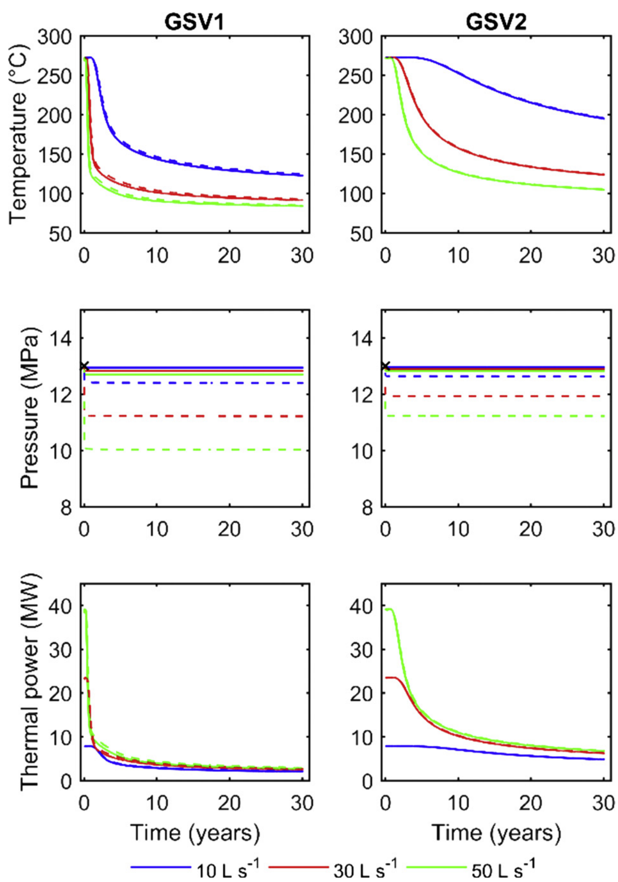

Fig. 10. Temperature (top), pressure (middle) and thermal power (bottom) for EGS in granite reservoir with volumes GSV1 (left) and GSV2 (right) as a function of time, injection rates and permeability, 10^{-12} m^2 (solid lines) and 10^{-13} m^2 (dashed lines). The initial pressure is indicated by a black cross on the y axis.

other providing similar thermal outputs, the reservoir impedance values in case of low permeability exceeds the threshold of 100 k Pa s L^{-1} (Table 5), which indicates no feasibility for an economic production (e.g., Clauser, 2006).

5.3.2. Granite Reservoir

The simulated temperature, pressure and thermal output for the stimulated volumes in granite are shown in Fig. 10. In the case of small stimulated volume of granite GSV1 (0.012 km^3), the temperatures corresponding to flow rates of 50 L s^{-1} and 30 L s^{-1} fall abruptly from 272 °C to less than 125 °C within the first few months of production. This sharp drop in temperature indicates quick cooling of the reservoir due to insufficient time and heat-exchange area required to heat up the injected water at that depth. The thermal power for a flow rate of 50 L s^{-1} reduces from maximal 40 MW in the first few months to less than 5 MW in 10 years. The generated average thermal power during this time period varies from 4.5 MW for an uneconomic flow rate of 10 L s^{-1} to 7.6 MW for a desired flow rate of 50 L s^{-1}.

Table 6
Reservoir impedance *i* for different simulated volumes *V*, permeability *k* and flow rates *Q* in granite.

V	*k* (m^2)	*Q* ($L\ s^{-1}$)	*i* ($kPa\ s\ L^{-1}$)
GSV1	10^{-12}	10/ 30/ 50	13.29/ 13.32/ 13.32
GSV1	10^{-13}	10/ 30/ 50	130.48/ 130.86/ 130.87
GSV2	10^{-12}	10/ 30/ 50	7.43/ 7.43/ 7.43
GSV2	10^{-13}	10/ 30/ 50	74.01/ 74.08/ 74.08

In GSV2, on the other hand, for circulation rate of 50 L s^{-1}, the temperature reaches 125 °C after gradually decreasing for 10 years and finally stabilizes slightly above 100 °C. For lower circulation rates of 30 L s^{-1} and 10 L s^{-1}, the temperature depletion is much slower and reaches 155 °C and 250 °C respectively after 10 years. During this time period, the generated mean thermal power varies between 7.7 MW for 10 L s^{-1} to 20.1 MW for 50 L s^{-1}. For the following 20 years, the mean thermal power output from the different scenarios stabilizes at approximately 8 MW for GSV2 as compared to 3 MW for GSV1. These numbers indicate that an increase of volume of the heat-exchanging zone by merely 30% lead to an increase of more than 100 % in the generated thermal power.

The thermal power production in GSV2 is also supported by the reservoir impedance values presented in Table 6. The initial pressure draw-down for a permeability of 10^{-12} m^2 is negligible, as compared to the draw-down corresponding to a permeability of 10^{-13} m^2.

6. Conclusion

Development of exploration geothermal fields is associated with significant geological and financial risks due to challenges related to unknown geological conditions. In such greenfield projects, assessment of uncertainty is crucial to decision making. Deterministic models based on sparse input data might result in biased and consequently invalid results.

To overcome these limitations, our minimum data approach uses a stochastic workflow to assess the sensitivity of the temperature field towards under-determined parameters. Besides allowing the identification of the most sensitive parameters that require further investigation through field or laboratory studies, this approach also provides more confident predictions that help to reduce the uncertainty and variability of the associated risk analysis.

From the Acoculco stochastic temperature modeling, three main conclusions can be drawn: (i) the assumptions of isotropic correlation lengths in granite and skarn, based on available information and geological considerations, do not show appreciable variations in mean temperature among the considered scenarios; (ii) thermal conductivity variation causes the maximum dispersion in simulated temperature profiles as compared to porosity, due to the very low porosity of host rocks (∼2 % and ∼1.2 % for granite and skarn respectively); (iii) stochastic results provide almost seven times higher confidence on the predicted temperature with respect to the deterministic models, as a result of a more realistic assignment of rock properties to grid cells, using the a-priori geological information introduced by the variogram input.

With regards to the production capacity, the results in skarn indicate that these volumes are not sufficient for commercial purposes. In order to avoid thermal breakthrough immediately within the first years of production, larger stimulated volumes need to be achieved. In the granite reservoir, on the contrary, profitable EGS operations are shown to be feasible with flow rates around 50 L s^{-1} and a stimulated volume equal or larger than the assumed stimulation zone. The ad-hoc stimulation volumes used in the current reservoir model set-up (0.012 km^3 and 0.036 km^3) are however conservative estimates of the possible heat exchange area in a real fracture network. As observed in GSV1 and GSV2, the volume achieved in the stimulation process has a stronger impact on the thermal power calculations than the assumed permeability of the stimulated zone. With more information on fracture density, fracture aperture and spacing, discrete fractures can be incorporated in the model, resulting in an increase in the effective heat exchange area and allowing an efficient heating up of injection fluid. This will consequently impact the prediction of thermal energy output and the life of a reservoir.

A limitation of the present case study is the assumption of no connectivity between the stimulated volume and the large regional faults due to limited knowledge of the geometry and the vertical extent of the faults. Communication of the stimulated zone with permeable faults in the vicinity would increase the volume of the stimulated area and affect the productivity of the field in general. This hypothesis can be tested in future works, if the existence of such geological discontinuities will be confirmed from other data sources (e.g. structural geological observations, natural CO_2 emission measurements, geophysical data, stimulation tests such as mini-fracking). Another factor which requires investigation is the induced seismicity rate related to injection and production, which has not been accounted for in this study.

CRediT authorship contribution statement

Paromita Deb: Conceptualization, Methodology, Software, Validation, Formal analysis, Writing - original draft, Writing - review & editing, Visualisation, Supervision, Project administration. **Dominique Knapp:** Methodology, Software, Formal analysis, Writing - review & editing. **Gabriele Marquart:** Supervision, Writing - review & editing. **Christoph Clauser:** Conceptualization, Supervision, Writing - review & editing, Project administration, Funding acquisition. **Eugenio Trumpy:** Methodology, Writing - review & editing.

Declaration of Competing Interest

The authors declare that they have no known competing financial interests or personal relationships that could have appeared to influence the work reported in this paper.

Acknowledgements

The project is funded European Union's Horizon 2020 research and innovation programme under grant agreement No. 727550. The authors thank the Comision Federal di Electricidad (CFE) for providing data and information regarding the geothermal wells and the entire GEMex consortium comprising of Mexican and European partners for the cooperation and unpublished inputs on conceptual ideas, which are used for this study.

References

Arellano, V.M., García, R.M., Barragán, G., Izquierdo, A., Araagón, A., Nieva, D., 2003. An updated conceptual model of the Los Humeros geothermal reservoir (Mexico). Journal of Volcanology and Geothermal Reserarch 124 (67-), 88.

Ascencio, F., Garcia, A., Rivera, J., Arellano, V., 1994. Estimation of undisturbed formation temperatures under spherical-radial heat flow conditions. Geothermics 23 (4), 317–326.

Avellán, D.R., Macías, J.L., Layer, P.W., Cisneros, G., Sánchez - Núñez, J.M., Gómez-Vasconcelos, Pola A., Sosa-Ceballos, G., García-Tenorio, F., Reyes-Agustín, G., Osorio-Ocampo, S., García-Sánchez, L., Mendiola, F., Marti, J., López-Loera, H., Benowitz, J., 2018. Geology of the Late Pliocene – Pleistocene Acoculco caldera complex, eastern Trans-Mexican Volcanic Belt (México). Journal of Maps. https://doi.org/10.1080/17445647.2018.1531075.

Baujard, C., Genter, A., Dalmais, E., Maurer, V., Hehn, R., Rosillette, R., Vidal, J., Schmittbuhl, J., 2017. Hydrothermal characterization of wells GRT-1 and GRT-2 in Rittershoffen, France: Implications on the understanding of natural flow systems in the rhine graben. Geothermics 65, 255–268. https://doi.org/10.1016/j.geothermics.2016.11.001.

Bär, K., Weydt, L., Deb, P., Kummerow, J., Ferrero, A., Vagnon, F., Colombero, C., Chicco, J., Vinciguerra, S., Siegfried, R., Comina, C., Mandrone, G., Laciska, A., Kemp, S., Kilpatrick, A., Rochelle, C., Milsch, H., Vacha, D., Rushton, J., 2019. Comprehensive report on the rock and fluid samples and their physical properties in the Acoculco and Los Humeros regions. GEMex – H2020 project report D6.1. . https://data.d4science.net/zVLc.

Brown, D.W., Duchane, D.V., Heiken, G., Hriscu, V.Th., 2012. The enormous potential for Hot Dry Rock geothermal energy. Mining the Earth's Heat: Hot Dry Rock Geothermal Energy. Springer-Publishing, Berlin Heidelberg, pp. 17–39.

Calcagno, P., Evanno, G., Trumpy, E., Gutiérrez-Negrín, L.C., Macías, J.L., Carrasco-Núñez, G., Liotta, D., 2018. Preliminary 3-D geological models of Los Humeros and Acoculco geothermal fields (Mexico) – H2020GEMex Project. Advances in Geosciences 45, 321–333.

Calcagno, P., Trumpy, E., Gutiérrez-Negrín, L.C., Norini, G., Macías, J.L., Carrasco-Núñez, G., Liotta, D., Garduño-Monroy, V.H., Hersir, G.P., Vaessen, L., Evanno, G., Arango Galván, C., 2021. Updating the 3D Geomodels of Los Humeros and Acoculco Geothermal Systems (Mexico) – H2020 GEMex Project. World Geothermal Congress proceedings (accepted).

Chiozzi, P., Barkaoui, A.-E., Rimi, A., Verdoya, M., Zarhloule, Y., 2017. A review of surface heat-flow data of the northern Middle Atlas (Morocco). Journal of Geodynamics 112, 58–71.

Clauser, C. (Ed.), 2003. Numerical Simulation of Reactive Flow in Hot Aquifers SHEMAT and PROCESSING SHEMAT. Springer-Publishing, Berlin Heidelberg.

Clauser, C., 2006. Geothermal energy. In: Heinloth, K. (Ed.), Landolt-Börnstein, Group VIII: Advanced Material and Technologies, 3, Energy Technologies, Subvol. C: Renewable Energies. Springer Verlag, Heidelberg-Berlin, pp. 566–594. https://doi.org/10.1007/10858992_20.

Deb, P., Knapp, D., Marquart, G., Montegrossi, G., 2019. Report on the calibrated reservoir model for the super-hot reservoir at Los Humeros and its calibration against available field data. GEMex – H2020 project report D6.1. . https://data.d4science.net/xhNC.

Deutsch, C.V., Journel, A.G., 1998. GSLIB. Geostatistical software library and user's guide. University Press, Oxford.

Heidbach, O., Rajabi, M., Reiter, K., Ziegler, M., 2016. World Stress Map 2016. GFZ Data Services. https://doi.org/10.5880/WSM.2016.002.

Hogarth, R., Holl, H.-G., 2017. Lessons learned from the Habanero EGS Project. Geothermal Resources Council Transactions 41 pp. 13p.

Jolie, E., Bruhn, D., Hernández, A.L., Liotta, D., Garduño-Monroy, H., Lelli, M., Hersir, G.P., Arango-Galván, C., Bonté, D., Calcagno, P., Deb, P., Clauser, C., Peters, E., Ochoa, A.F.H., Huenges, E., González Acevedo, Z.I., Kieling, K., Trumpy, E., Vargas, J., Carlos Gutiérrez-Negrín, L., Aragón-Aguilar, A., Halldórsdóttir, S., González Partida, E., Van Wees, J.-D., Angel, M., Montes, R., Didier, H., León, D., Team, G., 2018. GEMex – A Mexican-European research cooperation on development of superhot and engineered geothermal systems. Proceedings Geothermal Reservoir Engineering Stanford University 1–10.

Kölbel, T., Genter, A., 2017. Enhanced Geothermal Systems: The Soultz-sous-Forêts Project. In: Uyar, T. (Ed.), Towards 100% Renewable Energy. Springer Int. Publishings, pp. 243–248.

Kolditz, O., Clauser, C., 1998. Numerical simulation of flow and heat transfer in fractured crystalline rocks: application to the hot dry rock site in Rosemanowes (U.K.). Geothermics 27 (1), 1–23.

Langella, G., Paoletti, V., DiPippo, R., Amoresanoa, A., Steinunnardóttir, K., Milano, M., 2017. Krafla geothermal system, northeastern Iceland: Performance assessment of alternative plant configurations. Geothermics 169, 74–92.

Lee, Y., Deming, D., 1998. Evaluation of thermal conductivity temperature corrections applied in terrestrial heat flow studies. Journal of Geophysical Research 103 (B2), 2447–2454.

Li, Mengying, Lior, Noam, 2014. Comparative analysis of powerplant options for Enhanced geothermal Systems (EGS). Energies 7, 8427–8445. https://doi.org/10.3390/en7128427.

Liotta, et al., 2019. Final report on active systems: Los Humeros and Acoculco. GEMex Report D 4.1. . https://data.d4science.net/zd3S.

Llanos, E.M., Zarrouk, S.J., Hogarth, R.A., 2015. Simulation of the Habanero Enhanced Geothermal System (EGS), Australia. In: Proceedings World Geothermal Congress. Melbourne, Australia.

López-Hernández, A., García-Estrada, G., Aguirre-Díaz, G., González-Partida, E., Palma-Guzmán, H., Quijano-Léon, J.L., 2009. Hydrothermal activity in the Tulancingo-Acoculco Caldera Complex, central Mexico: Exploratory studies. Geothermics 38, 279–293.

Megel, T., Rybach, L., 2000. Production capacity and sustainability of geothermal doublets. In: Proceedings World Geothermal Congress. Kyushu – Tohoku, Japan.

Minissale, A., 1991. The Larderello geothermal field: a review. Earth-Sci. Rev. 31, 133–151.

MIT, 2006. The future of geothermal energy: impact of enhanced geothermal systems (EGS) on the United States in the 21st century. Report MIT. Available online. Massachusetts Institute of Technology, Cambridge, Massachusetts. https://www1.eere.energy.gov/geothermal/pdfs/future_geo_energy.pdf.

Norini, G., Carrasco-Núñez, G., Corbo-Camargo, F., Lermo, J., Hernández Rojas, J., Castro, C., Bonini, M., Montanari, D., Corti, G., Moratti, G., Piccardi, L., Chavez, G., Zuluaga, M.C., Ramirez, M., Cedillo, F., 2019. The structural architecture of the Los Humeros volcanic complex and geothermal field. Journal of Volcanology and Geothermal Research 381, 312–329. https://doi.org/10.1016/j.jvolgeores.2019.06.010.

Peaceman, D.W., 1983. Interpretation of well-block pressure in numerical reservoir simulation with non-square grid blocks and anisotropic permeability. Society of Petroleum Engineers Journal 23 (3), 531–543.

Polak, B.G., Prasolov, E.M., Kononov, V.I., Verkhovskiy, A.B., Gonzalez, A., Templos, L.A., Espindola, J.M., Arellano, J.M., Manon, A., 1982. Isotopic composition and

concentration of inert gases in Mexican hydrothermal systems. Geofisca International 21 ISSN 0016–7169.
Pulido, C.L., Flores Armenta, M.F., Silva, G.R., 2010. Characterization of the Acoculco Geothermal Zone as HDR System. Geothermal Resources Council Transactions 34, 369–372.
Rath, V., Wolf, A., Bücker, M., 2006. Joint three-dimensional inversion of coupled groundwater flow and heat transfer based on automatic differentiation: sensitivity, calculation, verification, and synthetic examples. Geophys. J. Int. 167, 453–466.
Reinicke, A., 2009. Mechanical and Hydraulic Aspects of Rock-Proppant Systems: Laboratory Experiments and Modelling Approaches. Doctoral Dissertation. University of Potsdam, Potsdam.
Rybach, L., 1976. Radioactive Heat Production: A Physical Property Determined by the Chemistry of Rocks. In: Strens, R.G.J. (Ed.), The Physics and Chemistry of Minerals and Rocks. Wiley & Sons, London, pp. 309–318.
Rybach, L., 1986. Amount and Significance of Radioactive Heat Sources in Sediments. In: Burrus, J. (Ed.), Thermal Modelling in Sedimentary Basins. Editions Technip, pp. 311–322.
Sanyal, S.K., Butler, S.J., 2005. An Analysis of Power Generation Prospects from Enhanced Geothermal Systems. In: Proceedings World Geothermal Congress. Antalya, Turkey.
Schön, J.H., 2004. Physical Properties of Rocks: Fundamentals and Principles of Petrophysics, 1. Edition. Elsevier, Amsterdam.
Sekiguchi, K., 1984. A method for determining terrestrial heat flow in oil basin areas. Tectonophysics 103, 67–79.
Vogt, C., Marquart, G., Kosack, C., Wolf, A., Clauser, C., 2012. Estimating the permeability distribution and its uncertainty at the EGS demonstration reservoir Soultz-sous-Forêts using the ensemble Kalman filter. Water Resources Research 48, W08517. https://doi.org/10.1029/2011WR011673.
Vogt, C., 2013. Optimization of geothermal energy reservoir modeling using advanced numerical tools for stochastic parameter estimation and quantifying uncertainties. Doctoral Dissertation. RWTH Aachen University, Aachen URN: urn:nbn:de:hbz:82-opus-45088.
Wagner, W., Cooper, J., Dittmann, A., Kijima, J., Kretzschmar, H., Kruse, A., Mares, R., Oguchi, K., Sato, H., Stocker, I., Sifner, O., Takaishi, Y., Tanishita, I., Trubenbach, J., Willkommen, T., 2000. The IAPWS industrial formulation 1997 for the thermodynamic properties of water and steam. J Eng Gas Turbines Power Trans ASME. 122 (1), 150–182. https://doi.org/10.1115/1.483186.
Ziagos, J.P., Blackwell, D.D., Mooser, F., 1985. Heat Flow in Southern Mexico and the Thermal Effects of Subduction. Journal of Geophysical Research 90, 5410–5420.
Zoth, G., Hänel, R., 1988. Appendix: 10.1. Thermal Conductivity. In: Hänel, R., Rybach, L., Stegna, L. (Eds.), Handbook of terrestrial heat flow density determination. Kluwer Academic Publishers, Dordrecht, pp. 447–468.

Web References

https://commons.wikimedia.org/wiki/File:Eje_Neovolc%C3%A1nico_Mexico.jpg, Last Accessed 06 March 2019
https://www.inegi.org.mx/app/geo2/elevacionesmex/, Last Accessed 14 Nov 2019,